ACS NANO
Cite This: ACS Nano 2018, 12, 4744−4753
www.acsnano.org

ARTICLE

Autonomous Thermal-Oxidative Composition Inversion and Texture Tuning of Liquid Metal Surfaces

Joel Cutinho,[†] Boyce S. Chang,[†] Stephanie Oyola-Reynoso,[†] Jiahao Chen,[†,‡] S. Sabrina Akhter,[§] Ian D. Tevis,[†] Nelson J. Bello,[§] Andrew Martin,[†] Michelle C. Foster,[§] and Martin M. Thuo*[,†,‡,∥]

[†]Department of Materials Science and Engineering, Iowa State University, 2220 Hoover Hall, Ames, Iowa 50011, United States
[‡]Microelectronics Research Center, Iowa State University, 133 Applied Sciences Complex I, 1925 Scholl Road, Ames, Iowa 50011, United States
[§]Department of Chemistry, University of Massachusetts Boston, 100 Morrissey Blvd., Boston, Massachusetts 02169, United States
[∥]Biopolymer and Bio-composites Research Team, Center for Bioplastics and Bio-composites, Iowa State University, 1041 Food Sciences Building, Ames, Iowa 50011, United States

Supporting Information

ABSTRACT: **Droplets capture an environment-dictated equilibrium state of a liquid material. Equilibrium, however, often necessitates nanoscale interface organization, especially with formation of a passivating layer. Herein, we demonstrate that this kinetics-driven organization may predispose a material to autonomous thermal-oxidative composition inversion (TOCI) and texture reconfiguration under felicitous choice of trigger. We exploit inherent structural complexity, differential reactivity, and metastability of the ultrathin (∼0.7−3 nm) passivating oxide layer on eutectic gallium−indium (EGaIn, 75.5% Ga, 24.5% In w/w) core−shell particles to illustrate this approach to surface engineering. Two tiers of texture can be produced after ca. 15 min of heating, with the first evolution showing crumpling, while the second is a particulate growth above the first uniform texture. The formation of tier 1 texture occurs primarily because of diffusion-driven oxide buildup, which, as expected, increases stiffness of the oxide layer. The surface of this tier is rich in Ga, akin to the ambient formed passivating oxide. Tier 2 occurs at higher temperature because of thermally triggered fracture of the now thick and stiff oxide shell. This process leads to inversion in composition of the surface oxide due to higher In content on the tier 2 features. At higher temperatures (≥800 °C), significant changes in composition lead to solidification of the remaining material. Volume change upon oxidation and solidification leads to a hollow structure with a textured surface and faceted core. Controlled thermal treatment of liquid EGaIn therefore leads to tunable surface roughness, composition inversion, increased stiffness in the oxide shell, or a porous solid structure. We infer that this tunability is due to the structure of the passivating oxide layer that is driven by differences in reactivity of Ga and In and requisite enrichment of the less reactive component at the metal−oxide interface.**

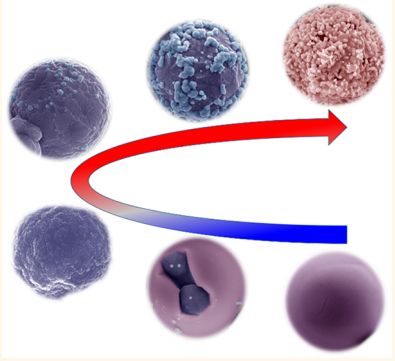

KEYWORDS: *passivating oxide, composition inversion, surface engineering, liquid metal, thermal oxidation, TOCI, nanointerface*

The shape and surface of liquid droplets are, by definition, a manifestation of a thermodynamically equilibrated state of fluid material(s).[1,2] Mechanical equilibrium, however, requires that pressure in the droplet be greater than that of its environment—the so-called Laplace pressure jump condition[3] which is size-dependent ($\Delta P = 2\gamma_{int}/r$, where γ_{int} = interfacial surface tension and r = radius).[3] In a homogeneous nonreactive liquid, the nature of the interface is dominated by this pressure jump condition. For high vapor pressure homogeneous liquids, these interfaces are binary; that is, liquid dominates across the Gibbs dividing plane; hence, there is a positive interface excess, $\Gamma_i \geq 0$. Similarly, in low vapor pressure liquids, $\Gamma_i < 0$. When the liquid is reactive, for example in liquid metals where passivating oxide forms upon exposure to air, then $\Gamma_i \ll 0$; hence, interfaces are defined by (i) reactivity (and associated kinetics), (ii) interfacial surface energies, (iii) post-oxidation equilibration in the presence of a fresh interface, and (iv) processing conditions.[1,2] Liquid metal surfaces are, therefore, challenging to engineer because of the dynamic and complex nature of their interfaces. Ability to modify composition and texture of liquid metal surfaces,

Received: February 23, 2018
Accepted: April 12, 2018
Published: April 12, 2018

DOI: 10.1021/acsnano.8b01438
ACS Nano 2018, 12, 4744−4753

however, opens alternative pathway(s) to overcoming equilibrium-driven surface properties and extends the utility of these materials. The dissipative nature and plastic deformation of liquid surfaces present a "self-rectifying" deformable (chemical or mechanical stress) platform.[4] This self-adjusting property in liquid metals coupled with the existence of multiple dividing planes (interfaces across bulk metal−oxide and oxide−air interface) over a short distance (because the interfaces are ∼0.7−3 nm)[5,6] translates to a high chemical potential, μ, gradient. Presence of these complex structure can sometimes dictate the overall properties, and hence utility, of such materials. In eutectic gallium indium (EGaIn), for example, a passivating oxide layer allows the non-Newtonian liquid to form moldable droplets and, to a certain extent, resist deformation.[7−11] The complexity of such nanoscale interfaces on liquid metal establishes an interesting engineering platform, especially in creating surfaces with tunable texture and composition.

Background. A material's surface texture affects local surface area and surface energy and hence has tremendous effect on its utility.[1] The effect of surface texture has inspired advances like superhydrophobic/superhydrophilic and self-cleaning materials.[12−16] High surface area also affects adsorption of small molecules and particles, hence, potential applications in catalysis and drug delivery.[17−19] Most methods that modify surface texture are additive,[20−28] subtractive,[29−33] or a combination of both.[34−36] Additive methods rely on introduction of chemi- or physisorbed adducts on the surface, whereas subtractive methods achieve this goal by selective partial removal of material to alter surface features. In addition, top-down,[37−40] bottom-up,[41,42] and interfacial methods[43−45] are also utilized to obtain characteristic surface patterns. Most of these approaches, however, often require complicated surface chemistry, stringent processing conditions, and arduous procedures.

A simple route to engineer surface texture is the growth of oxides on metal substrates. Thermal treatment of metal substrates provides a straightforward and tunable method to grow oxides.[46−50] Nonetheless, the inherently high stiffness and differences in thermal expansivities pose significant challenges in surface modification. Liquid metals, however, provide an alternative because they form nanoscale oxide shells that, because of size effects, are compliant to stresses.[5,51−53] Eutectic gallium−indium (EGaIn: 75.5% Ga, 24.5% In w/w; mp ≈ 15.7 °C) has recently found applications in soft and stretchable electronics,[7,8,54−59] functional microparticles,[5,9,10,60−63] molecular electronics,[64−75] and functional devices.[59,76−78] EGaIn bears a thin (∼0.7−3 nm) passivating film of predominantly Ga_2O_3 on the surface, rendering the liquid metal non-Newtonian as described above.[5,9,10,60,62,63] The EGaIn passivating oxide layer has a graded oxide structure with the surface being primarily Ga_2O_3, with underlying layer(s) of Ga and In suboxides, beneath which segregated In metal has been observed.[11,79−83] This complex structure spontaneously forms to a thickness of ca. 0.7 nm[5] and can gradually grow up to 3 nm,[6] largely because of limited diffusion of oxygen. This complex self-sorting structure of the oxide presents an opportunity to autonomously engineer the surface properties of these particles in a manner consistent with the built-in chemical potential gradients. Coupling differences in chemical potential, standard reduction potentials, thermal expansivities, and kinetics could lead to complex surface textures and elemental distribution.

Herein, we demonstrate that temperature-driven oxidation of EGaIn core−shell particles can be utilized to form tunable surface texture and invert composition by taking advantage of the elasticity and interfacial metastability of the passivating oxide layer.[84] We further show that surface modification is achieved *via* two processes (Figure 1a): (i) expansion−induced diffusion-limited oxidation (EDO), and (ii) thermo-mechanical fracture leakage and oxidation (TFO). The core−shell particle consisting of an EGaIn core and a Ga_2O_3 shell are illustrated in gray, whereas segregated In is represented in white. We infer that the liquid metal core−shell particle undergoes EDO and TFO upon heat treatment, which consequently transforms its surface texture and composition (Figure 1b). We hypothesized, and demonstrate, that EDO precedes TFO with associated volumetric and thermal expansivity changes leading to different surface textures.

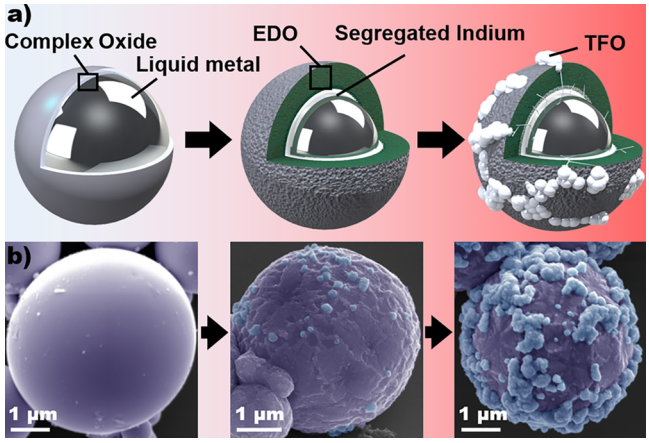

Figure 1. (a) Scheme outlining the possible pathways of oxide formation by thermal treatment. Oxide growth occurs *via* two competing routes, viz expansion-induced diffusion-limited oxidation (EDO) and/or thermo-mechanical fracture−leakage and oxidation (TFO) process. (b) Empirical validation of the proposed oxidation process.

RESULTS AND DISCUSSION

EGaIn core−shell particles synthesized using the shearing liquids into complex particles (SLICE) method[5] ranged between 1 and 5μm in diameter. Although the liquid core nature of the particle has been previously demonstrated,[52] this was further verified by the absence of phase segregation in the particles as observed by energy selective backscattered scanning electron microscopy (SEM). In addition, fractured particles flow and coalesce, confirming the liquid (fluidic) state of the core (Figures S1 and S2).

Effect of Temperature on Surface Texture. To investigate the effect of temperature on the particle surface, we performed heat treatment from ambient to 1273 K at 100 K increments. At each temperature increase starting at 573 K, the samples were allowed to equilibrate for 45 min before the cool-down cycle was initiated. Figure 2 illustrates changes in surface texture of EGaIn particles with temperature at different magnifications across the columns. Control EGaIn particles (Figures 2a−c and S1) exhibit smooth texture (purple) on the surface. Particles heat-treated at 573 K (300 °C) (Figure S3) appear smooth, albeit with observable surface deformations, suggesting that they have undergone anisotropic contraction.

DOI: 10.1021/acsnano.8b01438
ACS Nano 2018, 12, 4744−4753

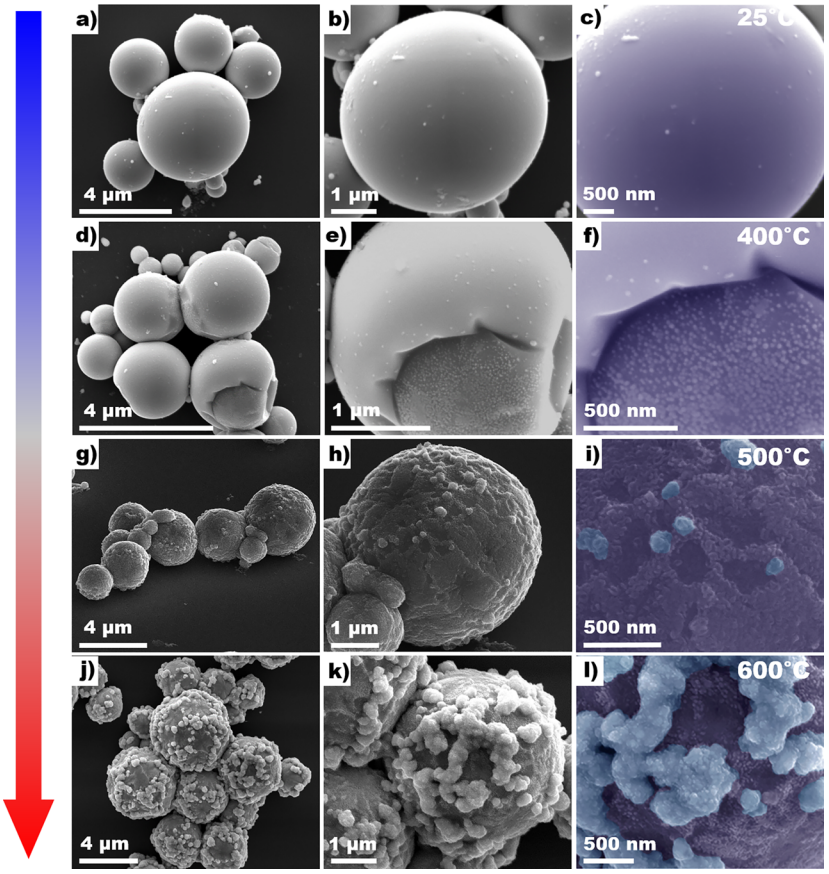

Figure 2. SEM images of EGaIn particles heat-treated at different temperatures under air atmosphere for 45 min. False coloring on high-magnification images highlights the different texture tiers observed on the surface. (a–c) Control EGaIn, (d–f) 400 °C, (g–i) 500 °C, and (j–l) 600 °C.

We infer that heating causes the shell layer to expand with concomitant increase in permeability to oxygen. This leads to accelerated growth of the oxide thickness.[6] Differences in thermal expansivity and elasticity of the thicker oxide would lead to stochastically distributed dimple-like defects upon cooling. This continuous oxide buildup is a manifestation of the EDO process. On the basis of reduction potentials and heats of formation,[85,86] we expect Ga to oxidize faster than In, leading to the formation of a thicker Ga_2O_3 layer,[6] with limited In_2O_3 beneath the surface. This buildup leads to concomitant enhancement of the previously observed interfacial chemical composition gradient.[79]

Significant changes in texture across the surface of the particles begin to appear at 400 °C (Figures 2d–f and S4) with the observation of rough regions on the particles. We speculate that this patchy growth is mediated by either mechanical fracture of the collapsed regions or buckling of the loose outer layers due to thermal stress. Particles treated at 500 °C (Figures 2g–i and S5) show considerable roughness without any buckling surface defects (dimples), a sign of uniformity in thermal contraction and likely increase in modulus of the oxide shell. We observe a nonuniform change in surface texture, as particle-like features appear on the surface. High-magnification images suggest that the texture is contributed by nanoridges, which we refer to as the first-tier texture (Figure S6). In addition, the false colored micrograph (Figure 2i) shows a second set of larger particles (of different chemical composition) lying on the surface, which we associate with the second-tier texture. We postulate that continuous expansion of the now thicker oxide shell coupled with constant oxide buildup (EDO), leads to fracture at a critical point (thermal stress > yield stress),[87,88] forcing the liquid to flow out (analogous to a volcano), a process we refer to as thermo-mechanical fracture leakage and oxidation (for brevity, TFO). Because increased surface oxidation leads to further phase enrichment of indium (either as the suboxide or elemental) underneath the oxide, we hypothesized that if microfractures lead to release of the bulk material, then the resulting oxides should have higher In content. This hypothesis is partially supported by contrast in the backscattered SEM images and is further evaluated below (Characterization and Compositional Analysis of the Surface). To further confirm that this process is thermally induced, we subjected the particles to a slightly higher temperature (~500 °C) in a dissipative environment and observed that the first tier of texture grows into volcano-like shapes that we infer are due to rapid growth of the oxide followed by contraction upon cooling to give these randomly distributed features. Under these conditions, however, the particles fracture because of the rapid cooling, but the liquid does not oxidize into specific structures (Figure S6).

At 600 °C (Figures 2j–l and S7), the second-tier material appears to grow extensively and cover the surface. This rapid growth is aided by thermal sintering, leading to a well-defined surface with two tiers of roughness. Backscattered SEM images (Figure S12) show significant contrast differences between the two tiers of texture, suggesting composition differences. Particles at 700 °C (Figure S8) and 800 °C (Figure S9) show continued growth of the second-tier texture, which

DOI: 10.1021/acsnano.8b01438
ACS Nano 2018, 12, 4744–4753

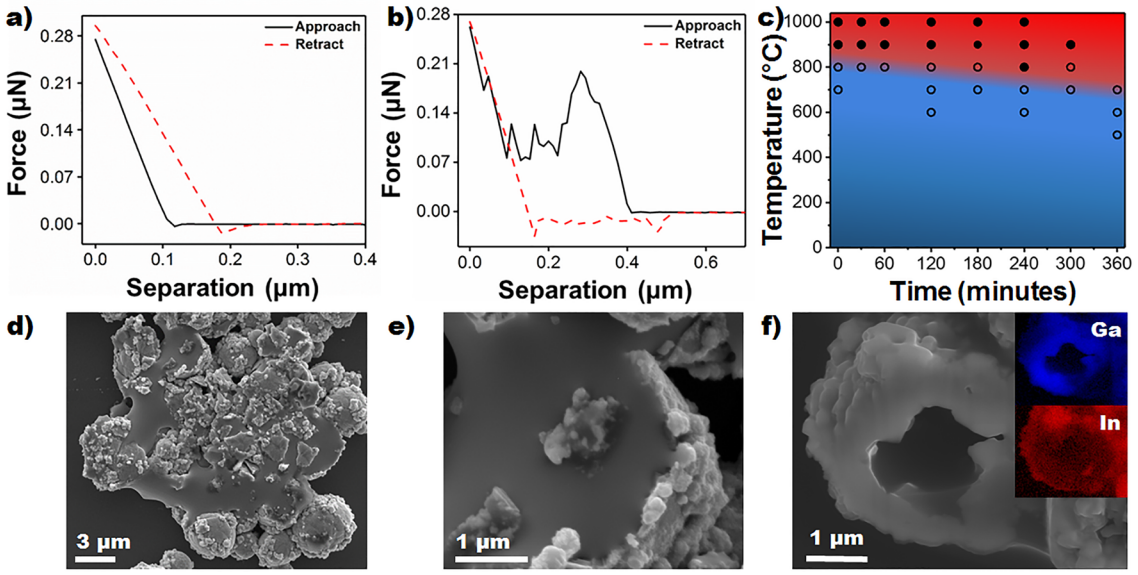

Figure 3. Assessment of the core of the particle. (a, b) AFM force−distance curves of particles heat-treated at 500 and 600 °C. (c) Temperature−time phase diagram showing the transition from liquid core to solid hollow core. (d) Fractured particles, heat treated at 600 °C for 60 min, shows that the core remains liquid after this heat treatment. (e) A magnification of the previous image outlining the broken fragments and thick oxide shell. (f) SEM micrograph with EDS map (insets) after ion milling of a particle heat-treated at 1000 °C for 120 min depicting a hollow cavity with facets, indicating growth of primarily Ga_2O_3 crystals beneath the shell.

ultimately leads to detachment from the parent particle. Finally, we observed another change in texture at 1000 °C (Figures S10 and S11), where the particles exhibit a high degree of coarsening as compared to lower temperatures. Furthermore, the appearance of polygonal facets in the core (observed from fractured particles, Figure S16) and the absence of liquid-like structures indicate that the material has oxidized substantially, if not completely (Figure 3f).

Thickening of the oxide is confirmed by changes in surface stiffness deduced from force−distance (F−D) curves (Figures 3a,b, S17, and S18). Force measurement using atomic force microscopy (AFM) shows at least 20% increase in stiffness from pristine to particles heat treated at 600 °C. Furthermore, sharp steps along the approach and not in the retraction F−D curve (Figure 3b) highlight the stiff and brittle nature of the shell. We therefore infer that at 600 °C (45 min), the oxide layer is brittle and hence likely to fracture, akin to bulk oxides. This result is in agreement with the onset of TFO, whereby the stiff oxide shell accumulates thermal stress and finally relaxes *via* fracturing leading to release of underlying material and hence formation of the second-tier texture (Figure 2j−l).

Liquid Metal to Solid Oxide Transition. To understand the liquid core to solid transition, we performed a series of heat treatment experiments ranging from 500 to 1000 °C held over various time scales. To reveal the core, we intentionally fractured the particles with a thin disposable needle after heat treatment to qualitatively determine if the core remains liquid (through observation of fluidic flow under SEM). Figure 3d,e depicts particles treated at 600 °C for 60 min at two different magnifications after deformation. In contrast to pristine EGaIn particles, thicker fractured oxide shells can be observed. An energy dispersive X-ray spectroscopy (EDS) elemental map of the cross section of broken particles (Figure S15) highlights the thickness of the oxide layer, which supports continuous growth. At higher temperatures (1000 °C), focused ion beam (FIB) milling reveals crystal-like facets in the core underneath the textured shell (Figures 3f and S16). We infer that oxidation coupled with crystallization is primarily responsible for the liquidless core. Total oxidation is expected to occur with increased permeability to oxygen and high reactivity of the heated metal. The oxidized nature of the material was confirmed using SEM-FIB and SEM-EDS, where the core of the particle appears to be hollow (Figure 3f). Unlike in the two-tier textures, breaching the passivation capability of the oxide leads to a mixed oxide species.

A systematic study at different processing temperatures and times was conducted to construct a temperature−time phase diagram (Figure 3c). We observed temperature-dominated transitions at 700−800 (t<3 hr) and 800−900 °C (t>3 hr), which can be attributed to the extent of oxidation as well as crystallization, both being temperature-dependent phenomena. As expected, the texture evolution changes oxygen permeability, especially with enhanced particle sintering. Figures S13 and S14 show particles with liquid and hollow cores at variable temperatures and times. We exercise caution in over-interpretation of this phase diagram and emphasize that the results shown here are highly dependent on experimental conditions.

Characterization and Compositional Analysis of the Surface. To confirm compositional differences between tier 1 and tier 2 textures, we characterize the surfaces using scanning Auger electron spectroscopy (AES) on control and heat-treated particles. The surface sensitivity of AES, coupled with the ability to map loci of different structural features *via in situ* SEM, enables differentiation of the two-tier textures. Figure 4 gives Auger spectra from point analysis performed on a control particle as well as the two-tiered morphological regions on a particle heat-treated at 600 °C (the survey scans of these particles are shown in Figure S19). Assignment and quantification of obtained peaks were based on literature values for Ga and In.[89−92] Comparison between pristine and heat-treated particles (tier 2) (Figure 4a,b) shows the emergence of an In MNN peak at 398 eV (Figure 4d) and a substantial decrease in the intensity of the C KVV peak at 262 eV (Figure

DOI: 10.1021/acsnano.8b01438
ACS Nano 2018, 12, 4744−4753

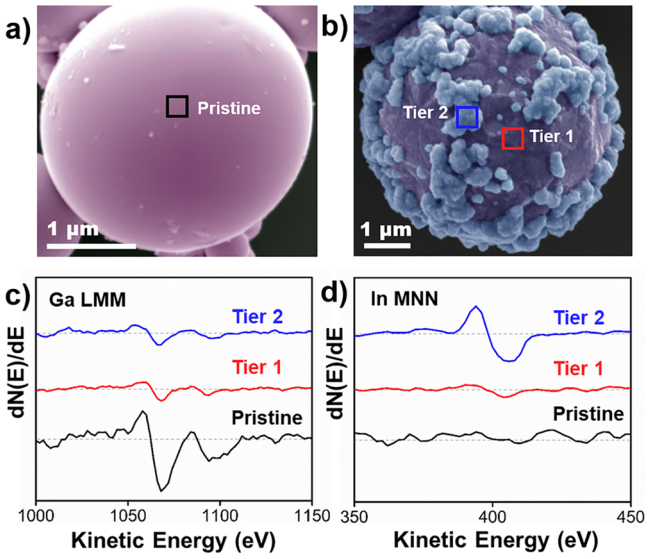

Figure 4. Composition of the surface of the particle. (a) False-colored SEM image of a control particle with point analysis on the surface. (b) False-colored SEM image of a particle treated at 600 °C with point analysis on the first- and second-tier roughness. (c) Auger spectroscopy of the Ga LMM region. (d) Auger spectroscopy of the In MNN region.

S19) in addition to the already present Ga LMM at 1063 eV (Figure 4c). The peak positions of Ga and In were approximately 5 eV lower than the metallic counterparts, indicating the formation of Ga_2O_3 and In_2O_3, respectively. These shifts are due to reduced electron density at the metal center, which in turn increases the binding energy of the remaining core electrons.[93−95] In contrast, tier 1 showed significantly less In, even though the intensity of Ga peak was comparable to that of tier 2. The enrichment of In likely originates from the underlying In-rich segregated layer that is released *via* TFO, as illustrated in Figure 1a.

Differentiation of Chemical Identity of the Two Tiers. Further X-ray photoelectron spectroscopy (XPS) analysis was performed on particles after heat treatments ranging from room temperature to 600 °C. Qualitative assessment of the peaks is summarized in the Supporting Information (Figures S20 and S21). We observed the presence of Ga^{3+} on all our samples (Figure 5a), whereas In^{3+} was not detectable until 400 °C (Figure 5b), which correlates well with SEM data. To obtain distinct spectra for both morphologies, we performed AES on both tiers. Figure 5c,d outlines the Auger spectra of the two tiers of texture separately (shown by the inset in both figures). We observed a greater peak height for In^{3+} from the spectra of tier 2, whereas tier 1 was dominated by Ga^{3+}. Figure S23a,b provides an estimate of relative composition between the two tiers based on peak-to-peak intensity of the differential spectra (details of the calculations are given in the Supporting Information). Elemental mapping with SEM-EDS for treated particles (600 °C) supports this observation (Figure S22).

Tuning Surface Texture and Composition by Thermal Treatment. *Composition Inversion.* The synergistic combination of metastable interface and flexibility of the liquid metal core−shell particles allows tuning of the surface texture and composition by thermal treatment. To quantify tier 2 morphology, we calculated peak areas from XPS spectra for In^{3+} as well as Ga^{3+}/In^{3+} ratio and plotted them against temperature (Figure 5e). To overcome any systematic errors in these measurements, we focus on the general trend in changes in composition rather than absolute concentrations. A decline in the ratio of Ga^{3+}/In^{3+} and increase in In^{3+} as temperature increases were observed (Figure 5e). These results confirm that tier 2 texture is In-enriched, indicating that the composition of the oxide layer has undergone an inversion as shown by comparison of the changes in surface concentration of In and Ga (Figure 5e).

Time−Temperature Compensation in Tunable Surface Coverage. Evolution of surface coverage of tier 2 with time (at 600 °C) showed modest growth (Figure 5f). This further supports the notion of a thermal expansion/reaction-initiated process. The duration of heat treatment, however, can be used to restructure the tier 2 morphology (Figure 5f), where islands of tier 2 morphology begin to form networks with increase in time. We therefore can infer that the overall surface texture can be tuned through felicitous choice of time−temperature conditions to generate a surface with desirable texture and Ga^{3+}/In^{3+} ratio.

Proposed Mechanism. We hypothesize that the process of thermal oxidation leading to change in surface texture depends on (i) diffusion of oxygen through the surface into the bulk, (ii) kinetics of the oxidation reaction, (iii) thermal expansion mismatch between the metal and oxide shell, and (iv) mechanical properties of the growing oxide. With increase in temperature, expansion of the elastic native oxide leads to an increase in oxygen permeability into the bulk—assuming Fickian transport (Wagner's theory).[96] An increase in diffusivity precedes oxidation into a native-like passivating oxide state. Although there was no observable significant surface texturing at 300 °C, surface dimples on the particles suggest an asymmetric change in the overall volume upon cooling. Conformity of the shell layer to a reduced volume of the core indicates that the shell layer is still elastic. Size-dominated properties are likely in effect, suggesting that the shell layer is still in the nanoscale and hence remains mechanically compliant.

For the oxidation of a curved oxide metal interface at high temperature, the stress at the interface (σ_i) depends on the difference in thermal expansivities of oxide and metal ($\Delta\alpha$), modulus of the oxide (E_{ox}), temperature difference (ΔT), particle radius (r), oxide thickness (ε), and Poisson's ratio for the oxide (ν_{ox}) as depicted in eq 1.[96]

$$\sigma_i = \frac{-\Delta\alpha\Delta T E_{ox}\varepsilon}{(1-\nu_{ox})} \quad (1)$$

Stress at the interface is compressive in nature during heating as opposed to the tensile stress on the oxide (σ_θ) (eq 2).[96] Thus, on the the basis of this model, if the stress in the oxide is lower than its failure stress, the oxide will continue to grow thicker *via* EDO as temperature predominantly increases oxygen permeability. With growth, however, the yield point transitions from that of the nanolayer (capable of plastic deformation) to that of the bulk (brittle). It is therefore expected that at a critical thickness, the oxide shell becomes brittle and subsequently fractures, releasing components of the immediate underlying layer.

$$\sigma_\theta = \frac{\Delta\alpha\Delta T E_{ox}}{(1-\nu_{ox})} \quad (2)$$

In our case, as Ga has a lower reduction potential (−0.55 V) and heat of formation,[87,88] it oxidizes faster than In (−0.34) to

DOI: 10.1021/acsnano.8b01438
ACS Nano 2018, 12, 4744−4753

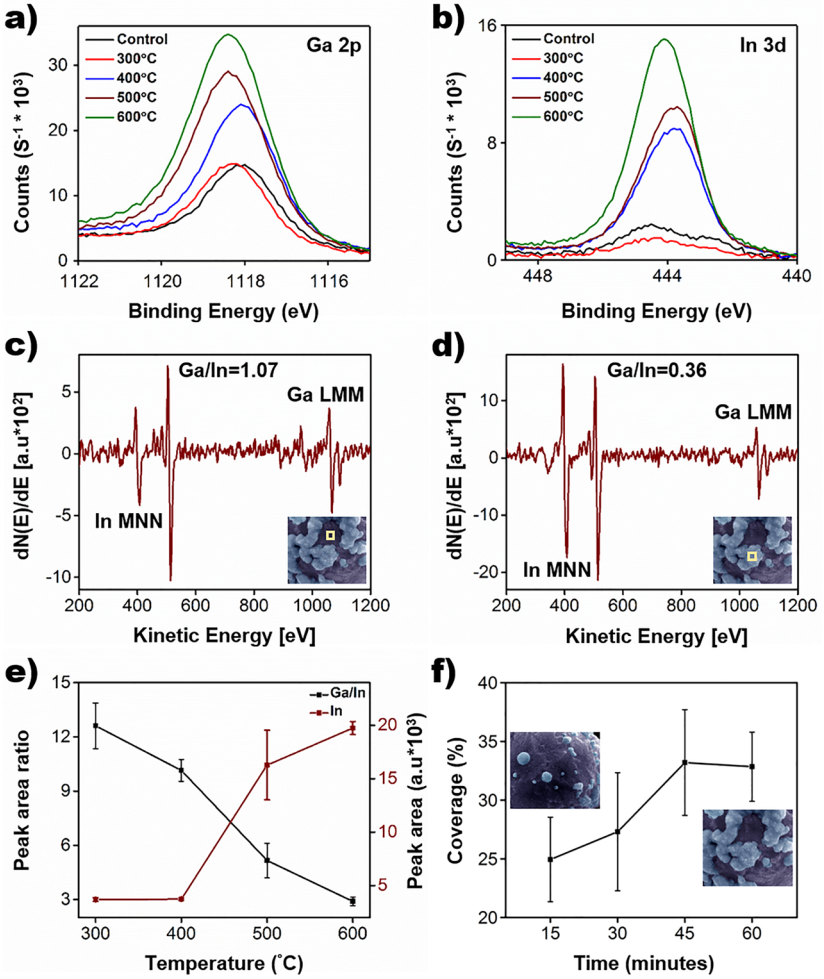

Figure 5. Growth and composition of the surface texture as captured by XPS and Auger spectroscopy. (a) XPS of the Ga $2p_{3/2}$ region at different temperatures. (b) XPS of the In $3d_{5/2}$ region at different temperatures. (c, d) Auger spectra survey collected from the two tiers of roughness on a particle treated at 600 °C. (e) Composition inversion of the surface components with temperature. (f) Coverage of tier 2 texture as a function of time.

seal the cracks and restructure the interface to form a Ga-rich surface. Analogous studies on Al nanoparticles showed significant restructuring after liquid Al leaked through cracks in the Al_2O_3 shell, albeit at a temperature beyond the melting point of Al.[97] Previous studies on titania rods have shown that freshly grown oxide is more fragile than the native passivating layer, which facilitates faster mechanical fracture and growth.[98] We can therefore assume that in our case subsequent layers grew rapidly after the first layer was fractured. Auger sputtering studies by Chiechi and co-workers concluded that the segregated layer of In is permeable to oxygen and that when fresh Ga_2O_3 is formed, it displaces In to the bottom.[11,80] Thus, repeated surface restructuring due to rapid oxidation of Ga at the surface leads to either an increase of In concentration at the core or its segregation at the interface to maintain the more stable eutectic composition. This In-enriched interface layer is released *via* surface fissures, which oxidizes to form the second-tier material. The formed materials then sinter to create a dominant network on the surface at higher temperatures. Thus, an inversion in the chemical identity of the surface, from the native Ga-rich to a mixed Ga/In or In-rich surface occurs. Considering the formation of an In-richer core, we shift to the hypereutectic point, which upon cooling gives rise to eutectic and In-rich phases in the core.[99] Characterization of the underlying In-rich phase and the relative composition of these two phases is beyond the scope of this study but has been described elsewhere.[79,83,100] At higher temperatures, however, a transition from liquid to solid core occurs because of accelerated diffusion of oxygen into the particle, which leads to complete oxidation and concomitant crystallization. Elemental mapping (SEM-EDS) shows a stochastic oxidation process at higher temperature (Figure 3f). Associated volumetric changes lead to a hollow core. Extensive surface coarsening and core faceting is an indication of complete crystallization of Ga_2O_3 and In_2O_3 at high temperatures (Figure S16).

CONCLUSION

This work demonstrates a facile, low-cost approach to engineer the surface texture of liquid metal particles *via* surface oxidation. We exploit interface organization and the associated metastability of EGaIn particles, coupled with the dynamic nature of the liquid metal core, to create textured liquid metal particles with concomitant composition inversion. Formation of phase-separated Ga-rich and In-rich oxides could find potential applications in the semiconducting industry or photocatalysis, where group 13 compounds have played a central role for band gap engineering. Specifically, we infer the following:

DOI: 10.1021/acsnano.8b01438
ACS Nano 2018, 12, 4744−4753

(i) *Thermally triggered oxidation induces surface roughness in a temperature-dependent manner:* The emergence and growth of surface texture is primarily dependent on thermal expansion mismatch between the liquid and native oxide. We achieve tunable surface texture and composition through felicitous choice of the substrate alloy and processing conditions.

(ii) *Tuning of surface texture can be accomplished without affecting composition.* Controlling heat treatment of EGaIn particles at moderate temperatures (<500 °C) induces texture change without significant change in oxide composition (Ga_2O_3) *via* expansion induced diffusion-limited oxidation.

(iii) *Mechanical stability of the oxide shell is enhanced.* EDO increases the thickness of the oxide shell, which transitions from flexible to stiff with increasing temperature. This increased mechanical strength of the oxide is in line with Wagner's diffusion-driven oxide growth.[96]

(iv) *An inversion in the composition of the surface occurs because of fracture-induced release of the underlying components.* The interfacial segregation of the low E° component (In) occurs with increased oxidant permeability. Fracture of the thickened oxide leads to release of an In-rich alloy, in part because of the interface In-enriched layer. Spontaneous oxidation of this alloy upon surface exposure leads to composition inversion of the most accessible surface components from the native Ga-rich to In-rich, although it is limited to the loci where the fracture occurs.

(v) *Oxidative phase and composition segregation occurs.* TFO results in a two-phase oxide at the surface: (1) Ga-rich phase formed due to EDO and (2) In-rich islands due to TFO, which engulf the surface at higher temperatures (>900 °C). Tier two features either sinter or fall off with increased growth.

(vi) *Maintaining a liquid core depends on processing time and temperature.* In general, as thermal oxidation of the liquid core leads to the growth and evolution of the surface, the nature of the core is tunable by varying processing temperature and time. Thus, higher temperatures and longer reaction times favor hollow particles, whereas the reverse is true for liquid core particles. In this study, we observed that a minimum of 800 °C is required for rapid formation of hollow particles, with longer reaction times needed at lower temperatures.

METHODS

Materials. Eutectic gallium–indium (Ga: In 75.5/24.5 wt %, Aldrich, ≥99.99% trace metal basis), glacial acetic acid (Fisher Scientific, Biotech, sequencing grade), and ethanol (Decon laboratories, 200 proof) were used as received for particle preparation and storage. A Thermo Scientific Smart2Pure 6 UV water purifier system was used to obtain deionized water.

Particle Preparation. We used a previously reported procedure to synthesize core–shell EGaIn@oxide@organic core–shell particles.[5] A 5 vol % solution of glacial acetic acid in deionized water (total: 100 mL) was placed into a Waring laboratory blender; 4 g of EGaIn were then added to the solution. The solution was sheared at 20 000 rpm for 10 min. Whatman 5 filter paper (1 μm particle retention) was used to isolate the particles through filtration. The particles were then rinsed and stored in ethanol.

Thermal Treatment. Thermal treatment was carried out either in a TGA (Q50 TA Instruments) or a tube furnace (Thermolyne 79300). Silicon wafer chips were washed with acetone and dried with ultrahigh-purity nitrogen gas. The particles were drop-casted onto a clean wafer, and the solvent was allowed to evaporate. Under an air environment, the TGA was conducted by placing the silicon wafer containing particles on a platinum pan. Gas flow and ramp rate were set at 50 mL/min and 10 °C/min, respectively. For the tube furnace experiments, the silicon wafers were placed on a ceramic crucible and carefully placed at the center of the tube followed by heating to target temperature. Following heat treatment, samples were cooled and maintained at ambient temperature prior to characterization. A control experiment without heat treatment was performed for comparison.

Characterization. All samples were imaged by scanning electron microscopy (FEI Quanta 250 FE-SEM). To observe internal microstructure, we utilized a focused ion beam (FEI Helios Nanolab DualBeam). False coloring was achieved using Adobe Photoshop. Elemental characterization was performed using energy dispersive X-ray spectroscopy and X-ray photoelectron spectroscopy (Kratos Amicus 3400). Force–displacement measurements were carried using atomic force microscopy (Bruker Innova AFM) under ambient conditions. To obtain elemental spectra for different morphological regions on the particle, scanning Auger microscopy (JEOL JAMP-7830F) was used. Further details of characterization are provided in the Supporting Information.

ASSOCIATED CONTENT

Supporting Information

The Supporting Information is available free of charge on the ACS Publications website at DOI: 10.1021/acsnano.8b01438.

SEM, FIB, AFM, XPS, and AES methods; SEM images of particles ranging from room temperature to 1000 °C and solid and hollow core particles; EDS map; FIB cross section of faceted core (1000 °C treated particles); force–displacement curve of room-temperature EGaIn particles; calculated stiffness of 500–600 °C particles; Auger electron spectra of room-temperature and 600 °C particles; calculation of Ga–In ratio from Auger spectra,;survey and deconvoluted XPS spectra of 600 °C particles (PDF)

AUTHOR INFORMATION

Corresponding Author

*E-mail: mthuo@iastate.edu.

ORCID

Jiahao Chen: 0000-0001-7563-8023

Martin M. Thuo: 0000-0003-3448-8027

Notes

The authors declare no competing financial interest.

ACKNOWLEDGMENTS

This work was supported by Iowa State University through startup funds and through a Black and Veatch faculty fellowship to M.M.T. S.O.-R. was supported in part by a GMAP fellowship from Iowa State University. Focused ion beam and Auger spectroscopy experiments were conducted at the Department of Energy's Ames National Laboratory Sensitive Instrument Facility. XPS experiments were performed at the Materials and Analysis Research Laboratory as well as the Ames Laboratory Sensitive Instrument Facility. We thank Dr. Dapeng Jing and Dr. James Anderegg for their help and support in XPS and Auger spectroscopy experiments, respectively. This work was carried out as part of J.C.'s graduate dissertation.[84]

DOI: 10.1021/acsnano.8b01438
ACS Nano 2018, 12, 4744–4753

REFERENCES

(1) Bormashenko, E. Y. *Wetting of Real Surfaces*. Walter de Gruyter: 2013; Vol. *19*.

(2) Butt, H.-J.; Graf, K.; Kappl, M. *Physics and Chemistry of Interfaces*, 3rd ed.; Wiley-VCH: 2013; p 495.

(3) Israelachvili, J. N. *Intermolecular and Surface Forces*; Academic Press: 2011.

(4) Shuttleworth, R. The Surface Tension of Solids. *Proc. Phys. Soc., London, Sect. A* **1950**, *63*, 444.

(5) Tevis, I. D.; Newcomb, L. B.; Thuo, M. Synthesis of Liquid Core–Shell Particles and Solid Patchy Multicomponent Particles by Shearing Liquids Into Complex Particles (SLICE). *Langmuir* **2014**, *30*, 14308.

(6) Farrell, Z. J.; Tabor, C. Control of Gallium Oxide Growth on Liquid Metal Eutectic Gallium/Indium Nanoparticles *via* Thiolation. *Langmuir* **2018**, *34*, 234–240.

(7) Boley, J. W.; White, E. L.; Kramer, R. K. Mechanically Sintered Gallium–Indium Nanoparticles. *Adv. Mater.* **2015**, *27*, 2355–2360.

(8) Kramer, R. K.; Majidi, C.; Wood, R. J. Masked Deposition of Gallium- Indium Alloys for Liquid- Embedded Elastomer Conductors. *Adv. Funct. Mater.* **2013**, *23*, 5292–5296.

(9) Thelen, J.; Dickey, M. D.; Ward, T. A Study of the Production and Reversible Stability of EGaIn Liquid Metal Microspheres using Flow Focusing. *Lab Chip* **2012**, *12*, 3961–3967.

(10) Mohammed, G. M.; Xenakis, A.; Dickey, M. Production of Liquid Metal Spheres by Molding. *Metals* **2014**, *4*, 465–476.

(11) Dickey, M. D.; Chiechi, R. C.; Larsen, R. J.; Weiss, E. A.; Weitz, D. A.; Whitesides, G. M. Eutectic Gallium-Indium (EGaIn): A Liquid Metal Alloy for the Formation of Stable Structures in Microchannels at Room Temperature. *Adv. Funct. Mater.* **2008**, *18*, 1097–1104.

(12) Banerjee, I.; Pangule, R. C.; Kane, R. S. Antifouling Coatings: Recent Developments in the Design of Surfaces That Prevent Fouling by Proteins, Bacteria, and Marine Organisms. *Adv. Mater.* **2011**, *23*, 690–718.

(13) Nurioglu, A. G.; Esteves, A. C. C.; De With, G. Non- Toxic, non- Biocide- Release Antifouling Coatings Based on Molecular Structure Design for Marine Applications. *J. Mater. Chem. B* **2015**, *3*, 6547–6570.

(14) Sahoo, B. N.; Kandasubramanian, B. Recent Progress in Fabrication and Characterisation of Hierarchical Biomimetic Superhydrophobic Structures. *RSC Adv.* **2014**, *4*, 22053–22093.

(15) Zhang, D.; Wang, L.; Qian, H.; Li, X. Superhydrophobic Surfaces for Corrosion Protection: A Review of Recent Progresses and Future Directions. *J. Coat. Technol. Res.* **2016**, *13*, 11–29.

(16) Simpson, J. T.; Hunter, S. R.; Aytug, T. Superhydrophobic Materials and Coatings: A Review. *Rep. Prog. Phys.* **2015**, *78*, 086501.

(17) Ahmad Nor, Y.; Niu, Y.; Karmakar, S.; Zhou, L.; Xu, C.; Zhang, J.; Zhang, H.; Yu, M.; Mahony, D.; Mitter, N.; Cooper, M. A.; Yu, C. Shaping Nanoparticles with Hydrophilic Compositions and Hydrophobic Properties as Nanocarriers for Antibiotic Delivery. *ACS Cent. Sci.* **2015**, *1*, 328.

(18) Chaudhary, U. *Synthesis of High Surface Area Nanomaterials and their Application in Catalysis*. Masters Thesis, Iowa State University, 2016.

(19) Yue, Q.; Zhang, Y.; Jiang, Y.; Li, J.; Zhang, H.; Yu, C.; Elzatahry, A. A.; Alghamdi, A.; Deng, Y.; Zhao, D. Nanoengineering of Core–Shell Magnetic Mesoporous Microspheres with Tunable Surface Roughness. *J. Am. Chem. Soc.* **2017**, *139*, 4954–4961.

(20) Grave, D. A.; Hughes, Z. R.; Robinson, J. A.; Medill, T. P.; Hollander, M. J.; Stump, A. L.; Labella, M.; Weng, X.; Wolfe, D. E. Process– Structure– Property Relations of Micron Thick Gd2O3 Films Deposited by Reactive Electron- Beam Physical Vapor Deposition (EB- PVD). *Surf. Coat. Technol.* **2012**, *206*, 3094–3103.

(21) Hu, H.; Singer, J. P.; Osuji, C. O. Morphology Development in Thin Films of a Lamellar Block Copolymer Deposited by Electrospray. *Macromolecules* **2014**, *47*, 5703–5710.

(22) Jain, A.; Weng, X.; Raghavan, S.; Vanmil, B. L.; Myers, T.; Redwing, J. M. Effect of Polarity on the Growth of InN Films by Metalorganic Chemical Vapor Deposition. *J. Appl. Phys.* **2008**, *104*, 053112.

(23) Oyola-Reynoso, S.; Tevis, I. D.; Chen, J.; Chang, B. S.; Cinar, S.; Bloch, J. F.; Thuo, M. M. Recruiting Physisorbed Water in Surface Polymerization for Bio- Inspired Materials of Tunable Hydrophobicity. *J. Mater. Chem. A* **2016**, *4*, 14729–14738.

(24) Pan, M.; Bai, G.; Liu, Y.; Hong, S.; Dravid, V. P.; Petford-Long, A. K. Effect of Deposition Temperature on Surface Morphology and Magnetic Properties in Epitaxial CoFe2O4 Thin Films Deposited by Metal Organic Chemical Vapor Deposition. *J. Appl. Phys.* **2010**, *107*, 043908.

(25) Vadakel, V.; Menon, C. Optical and Surface Morphological Studies on CuPcOC 8 Thin Films Prepared by Physical Vapour Deposition. *Mater. Sci.-Pol.* **2013**, *31*, 391–396.

(26) Vasilyev, V. Y.; Mogilnikov, K. P.; Song, Y. W. Nucleation and Growth of Pulsed CVD Ru Films from Tricarbonyl[η[sup 4]-cyclohexa-1,3-diene]ruthenium. *J. Electrochem. Soc.* **2008**, *155*, D763.

(27) Wu, M.; Yan, W.; Jing, J.; Wang, D.; Shi, L.; Zhang, L.; Wang, X.; Li, S.; Chen, H. Patterned LiNbO3 Thin Film Fabrication Basing Aqueous Precursor and the Study on Pattern Quality and Film Morphology. *J. Alloys Compd.* **2016**, *670*, 144–149.

(28) Zhang, F.; Wu, Q.; Zhang, Y.; Zhu, J.; Liu, N.; Yang, J.; Wang, X.; Hu, Z. Chemical Vapor Deposition Growth of InN Nanostructures: Morphology Regulation and Field Emission Properties. *Appl. Surf. Sci.* **2012**, *258*, 9701–9705.

(29) Chen, Y.; Chu, C.; Zhou, Y.; Ru, Y.; Chen, H.; Chen, F.; He, Q.; Zhang, Y.; Zhang, L.; Shi, J. Reversible Pore-Structure Evolution in Hollow Silica Nanocapsules: Large Pores for siRNA Delivery and Nanoparticle Collecting. *Small* **2011**, *7*, 2935.

(30) Gnaser, H. Nanostructures on Surfaces by Ion Irradiation. *Pure Appl. Chem.* **2011**, *83*, 2003.

(31) Teichmann, M.; Lorbeer, J.; Ziberi, B.; Frost, F.; Rauschenbach, B. Pattern Formation on Ge by Low Energy Ion Beam Erosion. *New J. Phys.* **2013**, *15*, 103029.

(32) Van Dijken, J. G.; Brett, M. J. Dry Etching of Copper Phthalocyanine Thin Films: Effects on Morphology and Surface Stoichiometry. *Molecules* **2012**, *17*, 10119.

(33) Ziberi, B.; Cornejo, M.; Frost, F.; Rauschenbach, B. Highly Ordered Nanopatterns on Ge and Si Surfaces by Ion Beam Sputtering. *J. Phys.: Condens. Matter* **2009**, *21*, 224003.

(34) Fang, J. S.; Lin, C. S.; Huang, Y. Y.; Chin, T. S. Surface-Morphology- Induced Hydrophobicity of Fluorocarbon Films Grown by a Simultaneous Etching and Deposition Process. *J. Electron. Mater.* **2015**, *44*, 2908–2914.

(35) Vázquez, L.; Buijnsters, J. G. Chemical and Physical Sputtering Effects on the Surface Morphology of Carbon Films Grown by Plasma Chemical Vapor Deposition. *J. Appl. Phys.* **2009**, *106*, 033504.

(36) Frankiewicz, C.; Attinger, D. Texture and Wettability of Metallic Lotus Leaves. *Nanoscale* **2016**, *8*, 3982–3990.

(37) Bratton, D.; Yang, D.; Dai, J.; Ober, C. K. Recent Progress in High Resolution Lithography. *Polym. Adv. Technol.* **2006**, *17*, 94–103.

(38) Zhou, L.; Dong, X.; Zhou, Y.; Su, W.; Chen, X.; Zhu, Y.; Shen, S. Multiscale Micro- Nano Nested Structures: Engineered Surface Morphology for Efficient Light Escaping in Organic Light- Emitting Diodes. *ACS Appl. Mater. Interfaces* **2015**, *7*, 26989.

(39) Ko, S. H. Low Temperature Thermal Engineering of Nanoparticle Ink for Flexible Electronics Applications. *Semicond. Sci. Technol.* **2016**, *31*, 073003.

(40) Zhang, W.; Krishnan, K. M. Epitaxial Patterning of Thin-Films: Conventional Lithographies and Beyond. *J. Micromech. Microeng.* **2014**, *24*, 093001.

(41) Chen, Y.; Fu, J.; Ng, K. C.; Tang, Y.; Cheng, W. Free-Standing Polymer–Nanoparticle Superlattice Sheets Self-Assembled at the Air–Liquid Interface. *Cryst. Growth Des.* **2011**, *11*, 4742–4746.

(42) Pang, M.; Cairns, A. J.; Liu, Y.; Belmabkhout, Y.; Zeng, H. C.; Eddaoudi, M. Synthesis and Integration of Fe-soc-MOF Cubes into Colloidosomes *via* a Single-Step Emulsion-Based Approach. *J. Am. Chem. Soc.* **2013**, *135*, 10234–10237.

DOI: 10.1021/acsnano.8b01438
ACS Nano 2018, 12, 4744–4753

(43) Hussain, M.; Xie, J.; Hou, Z.; Shezad, K.; Xu, J.; Wang, K.; Gao, Y.; Shen, L.; Zhu, J. Regulation of Drug Release by Tuning Surface Textures of Biodegradable Polymer Microparticles. *ACS Appl. Mater. Interfaces* **2017**, *9*, 14391−14400.
(44) Mason, B. P.; Bogdan, A. R.; Goswami, A.; McQuade, D. T. A General Approach to Creating Soluble Catalytic Polymers Heterogenized in Microcapsules. *Org. Lett.* **2007**, *9*, 3449.
(45) Price, K. E.; Broadwater, S. J.; Bogdan, A. R.; Keresztes, I.; Steinbacher, J. L.; McQuade, D. T. Self-Diffusion of Linear Polymers within Microcapsules. *Macromolecules* **2006**, *39*, 7681−7685.
(46) Cai, S. M.; Matsushita, T.; Fujii, H.; Shirai, K.; Nonomura, T.; Tatsuoka, H.; Hsu, C. W.; Wu, Y. J.; Chou, L. J. Growth of Cu- Oxide Nanowires on Cu Substrates by Thermal Annealing. *e-J. Surf. Sci. Nanotechnol.* **2012**, *10*, 175−179.
(47) Chalamala, B. R.; Wei, Y.; Reuss, R. H.; Aggarwal, S.; Gnade, B. E.; Ramesh, R.; Bernhard, J. M.; Sosa, E. D.; Golden, D. E. Effect of Growth Conditions on Surface Morphology and Photoelectric Work Function Characteristics of Iridium Oxide Thin Films. *Appl. Phys. Lett.* **1999**, *74*, 1394−1396.
(48) Inayat, A.; Makky, A.; Giraldo, J.; Kuhnt, A.; Busse, C.; Schwieger, W. Thermally Induced Growth of ZnO Nanocrystals on Mixed Metal Oxide Surfaces. *Chem. - Eur. J.* **2014**, *20*, 8161.
(49) Kawamura, K.; Motooka, T. Influence of Oxygen Partial Pressure on Thickness Change of Buried Oxide in Silicon-on-Insulator Structure during High- Temperature Oxidation Processes. *J. Electrochem. Soc.* **2006**, *153*, G1078.
(50) Martínez, O.; Hortelano, V.; Jiménez, J.; Plaza, J. L.; de Dios, S.; Olvera, J.; Diéguez, E.; Fath, R.; Lozano, J. G.; Ben, T.; González, D.; Mass, J. Growth of ZnO Nanowires Through Thermal Oxidation of Metallic Zinc Films on CdTe Substrates. *J. Alloys Compd.* **2011**, *509*, 5400−5407.
(51) Dickey, M. D. Emerging Applications of Liquid Metals Featuring Surface Oxides. *ACS Appl. Mater. Interfaces* **2014**, *6*, 18369−18379.
(52) Cinar, S.; Tevis, I. D.; Chen, J.; Thuo, M. Mechanical Fracturing of Core-Shell Undercooled Metal Particles for Heat-Free Soldering. *Sci. Rep.* **2016**, *6*, 21864.
(53) Chang, B. S.; Tutika, R.; Cutinho, J.; Oyola-Reynoso, S.; Chen, J.; Bartlett, M. D.; Thuo, M. M. Mechanically Triggered Composite Stiffness Tuning Through Thermodynamic Relaxation (ST3R). *Mater. Horiz.* **2018**, DOI: 10.1039/C8MH00032H.
(54) Dickey, M. D. Stretchable and Soft Electronics using Liquid Metals. *Adv. Mater.* **2017**, *29*, 1606425.
(55) Fassler, A.; Majidi, C. Liquid-Phase Metal Inclusions for a Conductive Polymer Composite. *Adv. Mater.* **2015**, *27*, 1928.
(56) Hirsch, A.; Michaud, H. O.; Gerratt, A. P.; de Mulatier, S.; Lacour, S. P. Intrinsically Stretchable Biphasic (Solid- Liquid) Thin Metal Films. *Adv. Mater.* **2016**, *28*, 4507.
(57) Jeong, S. H.; Hagman, A.; Hjort, K.; Jobs, M.; Sundqvist, J.; Wu, Z. Liquid Alloy Printing of Microfluidic Stretchable Electronics. *Lab Chip* **2012**, *12*, 4657.
(58) Li, G.; Wu, X.; Lee, D.-W. Selectively Plated Stretchable Liquid Metal Wires for Transparent Electronics. Sens. *Sens. Actuators, B* **2015**, *221*, 1114−1119.
(59) Lu, T.; Finkenauer, L.; Wissman, J.; Majidi, C. Rapid Prototyping for Soft- Matter Electronics. *Adv. Funct. Mater.* **2014**, *24*, 3351.
(60) Hohman, J. N.; Kim, M.; Wadsworth, G. A.; Bednar, H. R.; Jiang, J.; Lethai, M. A.; Weiss, P. S. Directing Substrate Morphology *via* Self-Assembly: Ligand-Mediated Scission of Gallium−Indium Microspheres to the Nanoscale. *Nano Lett.* **2011**, *11*, 5104.
(61) Lu, Y.; Hu, Q.; Lin, Y.; Pacardo, D. B.; Wang, C.; Sun, W.; Ligler, F. S.; Dickey, M. D.; Gu, Z. Transformable Liquid- Metal Nanomedicine. *Nat. Commun.* **2015**, *6*, 10066.
(62) Tang, S.-Y.; Joshipura, I. D.; Lin, Y.; Kalantar-Zadeh, K.; Mitchell, A.; Khoshmanesh, K.; Dickey, M. D. Liquid-Metal Microdroplets Formed Dynamically with Electrical Control of Size and Rate. *Adv. Mater.* **2016**, *28*, 604.
(63) Zhang, W.; Naidu, B. S.; Ou, J. Z.; O'Mullane, A. P.; Chrimes, A. F.; Carey, B. J.; Wang, Y.; Tang, S.-Y.; Sivan, V.; Mitchell, A.; Bhargava, S. K.; Kalantar-Zadeh, K. Liquid Metal/Metal Oxide Frameworks with Incorporated Ga2O3 for Photocatalysis. *ACS Appl. Mater. Interfaces* **2015**, *7*, 1943.
(64) Nijhuis, C. A.; Reus, W. F.; Whitesides, G. M. Molecular Rectification in Metal−SAM−Metal Oxide−Metal Junctions. *J. Am. Chem. Soc.* **2009**, *131*, 17814−17827.
(65) Simeone, F. C.; Barber, J. R.; Thuo, M. M.; Yoon, H. J.; Smith, B.; Whitesides, G. M. Defining the Value of Injection Current and Effective Electrical Contact Area for EGaIn-Based Molecular Tunneling Junctions. *J. Am. Chem. Soc.* **2013**, *135*, 18131−18144.
(66) Thuo, M. M.; Reus, W. F.; Nijhuis, C. A.; Barber, J. R.; Kim, C.; Schulz, M. D.; Whitesides, G. M. Odd−Even Effects in Charge Transport across Self-Assembled Monolayers. *J. Am. Chem. Soc.* **2011**, *133*, 2962−2975.
(67) Baghbanzadeh, M.; Simeone, F. C.; Bowers, C. M.; Liao, K.-C.; Thuo, M.; Baghbanzadeh, M.; Miller, M. S.; Carmichael, T. B.; Whitesides, G. M. Odd−Even Effects in Charge Transport across n-Alkanethiolate-Based SAMs. *J. Am. Chem. Soc.* **2014**, *136*, 16919−16925.
(68) Barber, J. R.; Yoon, H. J.; Bowers, C. M.; Thuo, M. M.; Breiten, B.; Gooding, D. M.; Whitesides, G. M. Influence of Environment on the Measurement of Rates of Charge Transport across AgTS/SAM//Ga2O3/EGaIn Junctions. *Chem. Mater.* **2014**, *26*, 3938−3947.
(69) Sporrer, J.; Chen, J.; Wang, Z.; Thuo, M. M. Revealing the Nature of Molecule−Electrode Contact in Tunneling Junctions Using Raw Data Heat Maps. *J. Phys. Chem. Lett.* **2015**, *6*, 4952−4958.
(70) Thuo, M. M.; Reus, W. F.; Simeone, F. C.; Kim, C.; Schulz, M. D.; Yoon, H. J.; Whitesides, G. M. Replacing− CH2CH2−with−CONH−Does Not Significantly Change Rates of Charge Transport through AgTS-SAM//Ga2O3/EGaIn Junctions. *J. Am. Chem. Soc.* **2012**, *134*, 10876−10884.
(71) Chen, J.; Gathiaka, S.; Wang, Z.; Thuo, M. Role of Molecular Dipoles in Charge Transport across Large Area Molecular Junctions Delineated Using Isomorphic Self-Assembled Monolayers. *J. Phys. Chem. C* **2017**, *121*, 23931−23938.
(72) Chen, J.; Giroux, T. J.; Nguyen, Y.; Kadoma, A. A.; Chang, B. S.; VanVeller, B.; Thuo, M. M. Understanding Interface (Odd-Even) Effects in Charge Tunneling using a Polished EGaIn Electrode. *Phys. Chem. Chem. Phys.* **2018**, *20*, 4864−4878.
(73) Kong, G. D.; Kim, M.; Cho, S. J.; Yoon, H. J. Gradients of Rectification: Tuning Molecular Electronic Devices by the Controlled Use of Different-Sized Diluents in Heterogeneous Self-Assembled Monolayers. *Angew. Chem., Int. Ed.* **2016**, *55*, 10307−10311.
(74) Kong, G. D.; Yoon, H. J. Influence of Air-Oxidation on Rectification in Thiol-Based Molecular Monolayers. *J. Electrochem. Soc.* **2016**, *163*, G115−G121.
(75) Byeon, S. E.; Kim, M.; Yoon, H. J. Maskless Arbitrary Writing of Molecular Tunnel Junctions. *ACS Appl. Mater. Interfaces* **2017**, *9*, 40556−40563.
(76) Koo, H.-J.; So, J.-H.; Dickey, M. D.; Velev, O. D. Towards All-Soft Matter Circuits: Prototypes of Quasi-Liquid Devices with Memristor Characteristics. *Adv. Mater.* **2011**, *23*, 3559.
(77) Mengüç, Y.; Park, Y.-L.; Pei, H.; Vogt, D.; Aubin, P. M.; Winchell, E.; Fluke, L.; Stirling, L.; Wood, R. J.; Walsh, C. J. Wearable Soft Sensing Suit for Human Gait Measurement. *Int. J. Robotics Res.* **2014**, *33*, 1748−1764.
(78) Yeo, J. C.; Kenry, J.; Yu, K. P.; Loh, Z.; Wang, C. T.; Lim, C. T. Triple-State Liquid-Based Microfluidic Tactile Sensor with High Flexibility, Durability, and Sensitivity. *ACS Sens.* **2016**, *1*, 543.
(79) Cademartiri, L.; Thuo, M. M.; Nijhuis, C. A.; Reus, W. F.; Tricard, S.; Barber, J. R.; Sodhi, R. N. S.; Brodersen, P.; Kim, C.; Chiechi, R. C.; Whitesides, G. M. Electrical Resistance of Ag TS − S(CH 2) n − 1 CH 3 //Ga 2 O 3/EGaIn Tunneling Junctions. *J. Phys. Chem. C* **2012**, *116*, 10848−10860.
(80) Chiechi, R. C.; Weiss, E. A.; Dickey, M. D.; Whitesides, G. M. Eutectic Gallium−Indium (EGaIn): A Moldable Liquid Metal for

DOI: 10.1021/acsnano.8b01438
ACS Nano 2018, 12, 4744−4753

Electrical Characterization of Self-Assembled Monolayers. *Angew. Chem., Int. Ed.* **2008**, *47*, 142.
(81) Regan, M. J.; Pershan, P. S.; Magnussen, O. M.; Ocko, B. M.; Deutsch, M.; Berman, L. E. X-ray Reflectivity Studies of Liquid Metal and Alloy Surfaces. *Phys. Rev. B: Condens. Matter Mater. Phys.* **1997**, *55*, 15874−15884.
(82) Tostmann, H.; Dimasi, E.; Ocko, B. M.; Deutsch, M.; Pershan, P. S. X-ray Studies of Liquid Metal Surfaces. *J. Non-Cryst. Solids* **1999**, *250*, 182−190.
(83) Dumke, M.; Tombrello, T.; Weller, R.; Housley, R.; Cirlin, E. Sputtering of the Gallium-Indium Eutectic Alloy in the Liquid Phase. *Surf. Sci.* **1983**, *124*, 407−422.
(84) Cutinho, J. *Tuning Surface Texture of Liquid Metal Particles by Exploiting Material Metastability*. Masters Thesis, Iowa State University, 2017.
(85) Chatterji, D.; Vest, R. W. Thermodynamic Properties of the System Indium-Oxygen. *J. Am. Ceram. Soc.* **1972**, *55*, 575−578.
(86) Klinedinst, K.; Stevenson, D. The Determination of the Standard Gibbs Energy of Formation of β-Gallium Sesquioxide from emf Measurements using an Yttria-Doped Thoria Electrolyte. *J. Chem. Thermodyn.* **1972**, *4*, 565−573.
(87) Leadbetter, A. J.; Newsham, D. M. T. Anharmonic Effects in the Thermodynamic Properties of Solids III. A Liquid Gallium Immersion Dilatometer for the Range 50−700 °C: Thermal Expansivities of Hg, Ga, NaCl and KCl. *J. Phys. C: Solid State Phys.* **1969**, *2*, 210−219.
(88) Orlandi, F.; Mezzadri, F.; Calestani, G.; Boschi, F.; Fornari, R. Thermal Expansion Coefficients of β-Ga2O3 Single Crystals. *Appl. Phys. Express* **2015**, *8*, 111101.
(89) Butt, D. P.; Park, Y.; Taylor, T. N. Thermal Vaporization and Deposition of Gallium Oxide in Hydrogen. *J. Nucl. Mater.* **1999**, *264*, 71−77.
(90) Jeong, J.; Moon, J.; Hong, J.; Kang, J. S.; Fukuda, Y.; Lee, Y. Characterization of Low-Resistivity Indium Oxide Films by Auger Electron Spectroscopy, X-ray Photoelectron Spectroscopy, and X-ray Diffraction and Correlation Between Their Properties, Composition, and Texture. *J. Vac. Sci. Technol., A* **1996**, *14*, 293−298.
(91) Püttner, R.; Sekushin, V.; Kaindl, G.; Liu, X.; Fukuzawa, H.; Ueda, K.; Tanaka, T.; Hoshino, M.; Tanaka, H. A Vibrationally Resolved C 1s− 1 Auger Spectrum of CO2. *J. Phys. B: At., Mol. Opt. Phys.* **2008**, *41*, 045103.
(92) Wanger, C.; Riggs, W.; Davis, L.; Moulder, J.; Muilenberg, G. *Handbook of X-ray Photoelectron Spectroscopy*; Perkin-Elmer Corporation, Physical Electronics Division Press: Eden Prairie, MN, 1979; pp 38−81.
(93) Lin, A. W.; Armstrong, N. R.; Kuwana, T. X-ray Photoelectron/Auger electron Spectroscopic Studies of Tin and Indium Metal Foils and Oxides. *Anal. Chem.* **1977**, *49*, 1228−1235.
(94) Wagner, C. Auger Parameter in Electron Spectroscopy for the Identification of Chemical Species. *Anal. Chem.* **1975**, *47*, 1201−1203.
(95) Haas, T. W.; Grant, J.; Dooley, G. J., III Chemical Effects in Auger Electron Spectroscopy. *J. Appl. Phys.* **1972**, *43*, 1853−1860.
(96) Evans, H. Stress Effects in High Temperature Oxidation of Metals. *Int. Mater. Rev.* **1995**, *40*, 1−40.
(97) Rai, A.; Lee, D.; Park, K.; Zachariah, M. R. Importance of Phase Change of Aluminum in Oxidation of Aluminum Nanoparticles. *J. Phys. Chem. B* **2004**, *108*, 14793.
(98) Rosenband, V. Thermo- Mechanical Aspects of the Heterogeneous Ignition of Metals. Combust. *Combust. Flame* **2004**, *137*, 366−375.
(99) Ravindra Reddy, S.; Hajra, J. P. Thermodynamics and Phase Equilibria in the System Ga-In using Multi-Parameter Functions. *CALPHAD: Comput. Coupling Phase Diagrams Thermochem.* **1993**, *17*, 151−156.
(100) Sodhi, R. N.; Brodersen, P.; Cademartiri, L.; Thuo, M. M.; Nijhuis, C. A. Surface and Buried Interface Layer Studies on Challenging Structures as Studied by ARXPS. *Surf. Interface Anal.* **2017**, *49*, 1309−1315.

DOI: 10.1021/acsnano.8b01438
ACS Nano 2018, 12, 4744−4753